RESEARCH

Numerical simulation of calcium dynamics dependent ATP degradation, IP$_3$ and NADH production due to obesity in a hepatocyte cell

Vedika Mishra[1] · **Neeru Adlakha**[1]

Abstract

Calcium (Ca^{2+}) signals have a crucial role in regulating various processes of almost every cell to maintain its structure and function. Calcium dynamics has been studied in various cells including hepatocytes by many researchers, but the mechanisms of calcium signals involved in regulation and dysregulation of various processes like ATP degradation rate, IP$_3$ and NADH production rate respectively in normal and obese cells are still poorly understood. In this paper, a reaction diffusion equation of calcium is employed to propose a model of calcium dynamics by coupling ATP degradation rate, IP$_3$ and NADH production rate in hepatocyte cells under normal and obese conditions. The processes like source influx, buffer, endoplasmic reticulum (ER), mitochondrial calcium uniporters (MCU) and Na$^+$/Ca^{2+} exchanger (NCX) have been incorporated in the model. Linear finite element method is used along spatial dimension, and Crank-Nicolson method is used along temporal dimension for numerical simulation. The results have been obtained for the normal hepatocyte cells and for cells due to obesity. The comparative study of these results reveal significant difference caused due to obesity in Ca^{2+} dynamics as well as in ATP degradation rate, IP$_3$ and NADH production rate.

Keywords Finite element method · SERCA · IP$_3$ · ATP · NADH · ER · Buffers

1 Introduction

Intracellular calcium plays a major role in controlling the functions of the liver like release of digestive enzymes, production of various proteins and hormones, etc. There are two types of cells in the liver: (a) parenchymal cells and (b) non-parenchymal cells [1]. Hepatocytes are cubical shaped epithelial cells with sides 10–20 μm. These cells belong to the category of parenchymal cells and constitute 70% part of the liver. These cells are larger

✉ Vedika Mishra
d20ma001@amhd.svnit.ac.in

Neeru Adlakha
nad@amhd.svnit.ac.in

1 Department of Mathematics, SVNIT, Surat 395007, Gujarat, India

than the other cells and thus occupy about 80% of volume of the organ. Hepatocytes perform many important functions of liver like metabolism, storage, digestion and bile production [2]. A complex and various spatio-temporal calcium organisations are involved in these variety of cellular functions. There are two types of sources, i.e., external and internal for calcium present in a cell. The plasma membrane releases extracellular calcium using channels. Internal calcium stores, viz. endoplasmic reticulum/sarcoplasmic reticulum, mitochondria, golgi bodies and acidic organelles, are rich sources of calcium. Ryanodine (RYR) and Inositol 1,4,5 triphosphate receptors (IP$_3$R) mediate calcium's release from internal stores as shown in Fig. 1. These are ligand operated channels. Cytosolic calcium concentration is approximately 0.1 μM at rest, and in internal stores such as the ER, it is around 500 μM. As high calcium concentration is toxic for the cells, the excess calcium from the cytosol is pumped back to internal stores using various pumps such as SERCA pumps and plasma membrane ATPases [3].

Mitochondria is involved in many important functions, viz. metabolism, Krebs cycle, generation of energy and fatty acids. It is also involved in spatial and temporal changes in the cytosolic calcium. Its influx and efflux affect the frequency and amplitude of
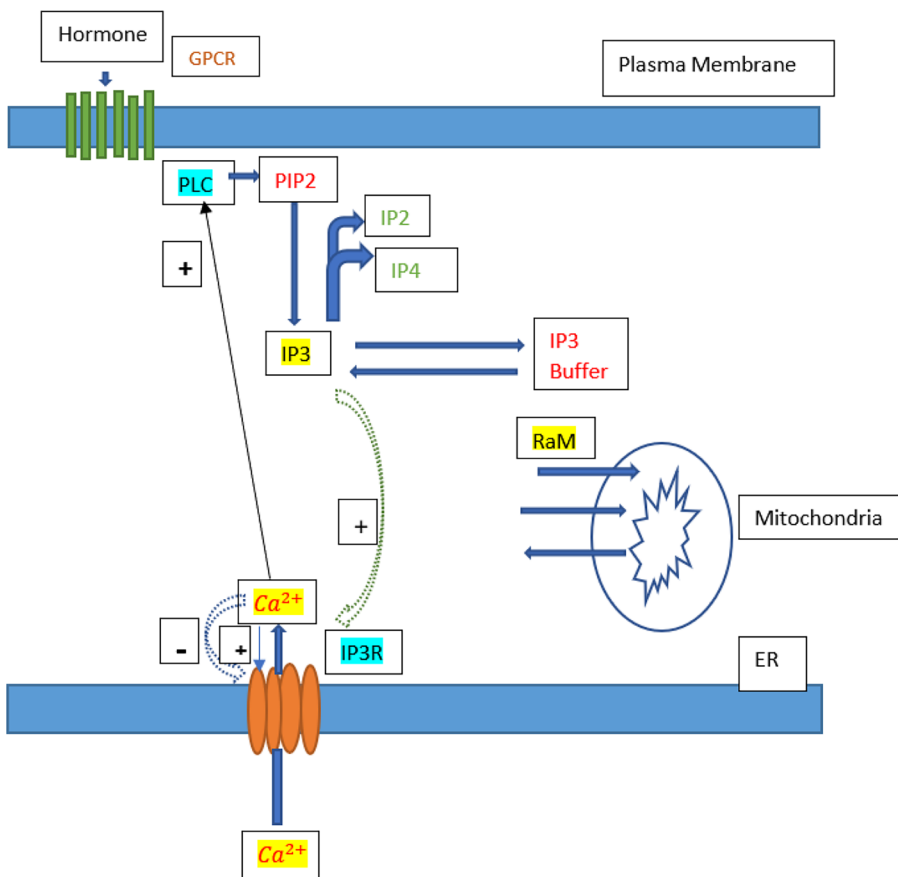

Fig. 1 Schematic diagram of the system

Ca^{2+} [4]. Mitochondria have the capacity to accumulate calcium using energy-dependent mechanism MCU, and they release calcium using NCX [5]. Two different kinds of NCX are found in animal cells, one in the mitochondria's inner membrane and the other in the outer membrane of the mitochondria. When mitochondria uptake calcium rapidly, it stimulates mitochondrial metabolism by stimulating rapid increase of NADH levels, ATP production and oxygen consumption [6].

Calcium signaling has been studied in various cells like neuron, oocyte, myocyte, astrocyte, pancreatic acinar and hepatocyte by various researchers [7–15]. Atri et al. [16] observed the intracellular calcium oscillation in fertilised oocytes. They constructed a mathematical model that can be used for any cell involving IP3R. Isshiki et al. [17] studied the behaviour of intracellular calcium concentration in endothelial cells. They used ATP for stimulation. It was observed that the calcium wave was dependent on intracellular calcium release, as Ca^{2+} wave was not affected when extracellular calcium was removed, and intervention by IP_3 was also observed . Salet et al. [18] studied calcium sequestering in the mitochondria of the liver and observed that a large amount of calcium has been taken by mitochondria. Berridge et al. [19] discussed calcium as a life and death signal. They concluded that cells perform different functions by selecting tool kit suitable to its work. It is involved in cell proliferation and apoptosis process. Kotwani et al. [8] have attempted to study one-dimensional calcium concentration variation in fibroblast cells involving excess buffers using finite difference method. Panday et al. [10] formulated a model for Ca^{2+} distribution involving NCX and advection of Ca^{2+} in oocytes. Naik et al. [7] studied the calcium distribution involving voltage-gated calcium channels (VGCC), RYR and buffers in oocytes. It was found that increase of Ca^{2+} concentration due to RYR was higher than that of VGCC. Nicholls [20] discussed the mitochondrial impact on the regulation of calcium loaded matrix of mitochondria in the process of dehydrogenases. They concluded that in the non-excitable cells, regulation of matrix dehydrogenase remains dominant in mitochondria, and in the excitable cells, the uptake of Ca^{2+} plays as a key regulatory role in mitochondrial processes. Selwyn et al. [21] discussed transport of calcium into the mitochondria using Ca^{2+}/H^+ exchangers which was intermediated by non-phosphorylated energy elements. Jha et al. [9] studied calcium distribution using finite element approach in astrocyte cells. Jagtap and Adlakha [11] studied calcium variation in a hepatocyte cell using finite volume method. They developed a steady state one-dimensional mathematical model using advection diffusion equation for calcium and IP_3. Jha et al. [12, 13, 22] observed the effects of NCX, source geometry, leak, SERCA pump etc. on Ca^{2+} oscillations in dendritic spines and neuron cells employing finite element approach. Pathak et al. [14] devised a mathematical model of calcium distribution in cardiac myocyte cells involving pump, excess buffer and leaks. Manhas et al. [15, 23] studied calcium variation in pancreatic acinar cells describing effects of mitochondria on Ca^{2+} signaling. Tewari and Pardasani [24, 25] have developed a model for neuron cells expressing impact of sodium pump on Ca^{2+} oscillation and calcium diffusion with excess buffer. They also formulated a mathematical model of tripartite synapses where astrocytes modulate short-term synaptic plasticity, consisting a pre-synaptic bouton, a post-synaptic dendritic spine-head, a synaptic cleft and a perisynaptic astrocyte controlling Ca^{2+} dynamics, inside the synaptic bouton [26]. Brumen et al. [27] studied calcium dynamics in airway smooth muscle cells using mathematical modelling involving intracellular Ca^{2+} stores such as sarcoplasmic reticulum and cytosolic proteins as well as Ca^{2+} exchange across the plasma membrane. Das et al. [28] built a four-dimensional model to mimic the cross-talk among plasma glucose, plasma insulin, intracellular glucose and cytoplasmic calcium of

a cardiomyocyte. They also studied the dynamic interaction of glucose-induced insulin secretion mechanism through glucose metabolism and ATP-dependent calcium influx by proposing and analysing a four-dimensional system of nonlinear delay differential equations to give insights into different possible mechanisms for maintaining plasma glucose homeostasis through calcium-induced insulin secretion for beta cells [29]. Das et al. [30] suggested a cardioprotective role of the MCU and predicted that a mitochondrial NCX could be a potential therapeutic target to restore the normal functioning of the cardiomyocytes. Colman et al. [31] developed an approach to model the sarcoplasmic reticulum structure at the whole-cell scale, by reducing its full 3-D structure to a 3-D network of one-dimensional strands for cardiac cells. Means and Sneyd [32] constructed a model of the spatio-temporal calcium dynamics within an interstitial cells of cajal pacemaker unit to determine under what conditions the local calcium concentrations may reduce below baseline. Paul et al. [33] proposed and analysed the glucose-stimulated insulin secretion process through a six-dimensional model incorporating calcium and ATP. Naik and Zu [34] developed a quantitative spatio-temporal Ca^{2+} dynamics model which includes the Ca^{2+} releasing channels ER leak and voltage-gated Ca^{2+} channel, buffering and reuptaking mechanism in the T lymphocytes. De Pittà et al. [35] studied the modulation of intracellular calcium dynamics in astrocytes in response to synaptic activity. Bianchi et al. [36] studied mechanism of Ca^{2+} transport, pathology and regulation of Ca^{2+} signaling in cell involving different sensors of mitochondrial calcium. Amaya and Nathanson [37] discussed molecular mechanism responsible for calcium signaling in the cytosol of hepatocyte cells. Babcock et al. [38] experimented and concluded that there is a active participation of mitochondria in intracellular calcium signaling. They also concluded that mitochondria has ability for rapid uptake and release of large amount of Ca^{2+}. Their study using ratiometric dyes discussed that low resting value of mitochondrial calcium is in the range of 80 to 200 nM for isolated as well as cellular mitochondria. Marhl et al. [39] studied calcium distribution involving mitochondria and buffers. They developed a compartmental model involving endoplasmic reticulum, mitochondria and buffers. Wacquier et al. [40] observed that ATP synthesis mechanism of mitochondria affects the frequencies and amplitudes of Ca^{2+} in the cell. Thomas et al. [41] studied calcium distribution in a hepatocyte cell along space and time dimension. Murphy et al. [42] studied effects of hormones on calcium variation in isolated hepatocyte cells. Dupont et al. [43] concluded that in a hepatocyte cell, repetitive calcium spikes occur with slight shift in phase with adjacent cells. Kothiya and Adlakha [44, 45] provided a mathematical model to analyse affects of Ca^{2+} signaling on the synthesis of ATP and IP_3 in fibroblast cells. Bhardwaj et al. [46] studied the nonlinear spatio-temporal dynamics of Ca^{2+} in T cells using a radial basis function-based differential quadrature technique involving the SERCA pump, RYR, source amplitude and buffers. Pawar et al. [47–51] studied interdependent calcium and IP_3 dynamics and its effect on nitric oxide production and β- amlyoid production and degradation. They also studied the interdependence of calcium, nitric oxide, dopamine and β- amlyoid.

Dysregulation in calcium signaling leads to various diseases, viz. obesity, insulin resistance and liver cholestasis. Obesity is a disease in which excess body fat accumulates and affects the health adversely. It is a heterogeneous group of disorder which has multiple causes. The upper body obesity is caused due to the intra-abdominal visceral disposition of adipose tissue which is responsible for development of hypertension, insulin resistance, hyperlipidaemia, hyperglycemia, diabetes mellitus and elevated plasma insulin concentrations [52]. Hyperglycemia increases the levels of free fatty acids causing lipotoxicity by accumulating fat on the myocytes, pancreatic β cells and hepatocytes. It also affects

intracellular signals [53]. ER dysfunction is also a result of obesity. In obesity, the ER becomes more leaky [54]. Han and Periwal [55] studied calcium dynamics in hepatocytes by constructing a compartmental model. They have also done a comparative study of calcium oscillations in control and obesity conditions.

The survey of literature gives a fair idea of the parameters incorporated by the researchers to study Ca^{2+} dynamics in various cells including hepatocytes. The hepatocyte cells constitute 70% cells of the liver and 80% volume of the liver. Thus, hepatocytes have a very crucial role in the functions of liver such as production and regulation of proteins and hormones required by various other organs of a human body. The calcium signaling is one of the key system of hepatocytes involved in these functions of the liver. Any disturbance or disruption in calcium signaling in hepatocytes can lead to various disorders of liver. The calcium signaling mechanisms in hepatocytes are still not well understood, and their insights are crucial for understanding the various disorders of the liver functions. However, very little work has been done by the past researchers to study the impacts of disturbances in the mechanisms of Ca^{2+} dynamics on the production of IP$_3$, degradation of ATP and production of NADH in normal and obese hepatocytes. The aim of the present study is to construct a mathematical model of calcium dynamics in hepatocytes involving source influx, buffers, SERCA pump, mitochondria and ER to explore their roles in ATP degradation, IP$_3$ and NADH production rate etc. in hepatocyte cells. Also, it is intended to explore the impacts of regulatory and dysregulatory mechanisms of calcium dynamics on ATP degradation rate, IP$_3$ and NADH production rate etc. levels in normal and obese hepatocyte cells to identify the conditions which can cause the liver disorders like obesity.

2 Mathematical formulation

The mathematical model proposed by Han and Periwal [55] is employed in the present study by incorporating diffusion term and excess buffers which is expressed as follows:

$$
\begin{aligned}
\frac{\partial[Ca^{2+}]}{\partial t} = {} & D_{Ca}\frac{\partial^2[Ca^{2+}]}{\partial x^2} + f_c[(1-R_{S1})(J_{IPR}-J_{SERCA}) \\
& + \frac{(1-R_{S2})}{R_{V3}}(J_{NCX}-J_{MCU}) + J_{diff} + J_{in} - J_{PM}] \\
& - k_j^+[B_j]_\infty([Ca^{2+}]-[Ca^{2+}]_\infty)
\end{aligned}
\tag{1}
$$

where D_{Ca} is diffusion coefficient, $[B_j]_\infty$ is total buffer concentration, R_{S1} and R_{S2} represent ratio of ER surface area adjoining mitochondrial-associated membrane (MAM) to the total surface area of ER and mitochondrial surface area adjoining the MAM to the total surface area of mitochondria respectively. R_{V3} represents ratio of total cytosolic volume to total mitochondrial volume. J_{IPR}, J_{SERCA}, J_{NCX}, J_{MCU}, J_{diff}, J_{in} and J_{PM} represent the cytosolic calcium flux through IP3R, Ca^{2+} flux from cytosol to ER via SERCA pump, flux through the NCX, influx of calcium in mitochondria via MCU, diffusion of calcium between MAMs and cytosol, total influx of calcium via store operated calcium channels (SOCC) and receptor operated calcium channels (ROCC) and a small constant influx (J_{leakin}) and efflux of calcium through plasma membrane Ca^{2+} ATPase respectively. $[Ca^{2+}]$ (dependent variable) represents calcium concentration in the cytosol of the hepatocytes. f_c represents fraction of free calcium present in the cytosol and k_j^+ is buffer association rate.

The following initial condition is imposed based on assumption that Ca^{2+} concentration at rest is 0.1 μM in the cell [11].

$$([Ca^{2+}]_{t=0}) = 0.1\,\mu M \tag{2}$$

The following boundary conditions based on the physical condition of source influx and assumption of background calcium concentration is maintained at other side of the boundary of the cell are imposed [11].

$$lim_{x \to 0}\left(-D_{Ca}\left(\frac{\partial[Ca^{2+}]}{\partial x}\right)\right) = \sigma_{Ca} \tag{3}$$

where σ_{Ca} represents source influx.

$$lim_{x \to 15}([Ca^{2+}]) = C_{\infty} = 0.1\,\mu M \tag{4}$$

The various fluxes are modelled as [23, 40, 55],

$$J_{IPR} = k_{IPR}O_{IPR}([Ca_{ER}] - [Ca^{2+}]) \tag{5}$$

where $[Ca_{ER}]$ is calcium concentration in ER, k_{IPR} represents receptor activity levels in the cytosol, and O_{IPR} is given by

$$O_{IPR} = \frac{q_{26}}{q_{62} + q_{26}}D \tag{6}$$

here O_{IPR} represents open probability of IP$_3$R in the cytosol. q_{26} and q_{62} are transition rate from C_2 to O_6 and transition rate from O_6 to C_2 respectively.

$$D = \frac{q_{42}(q_{62} + q_{26})}{q_{42}q_{62} + q_{42}q_{26} + q_{24}q_{62}} \tag{7}$$

D represents the proportions of the IP$_3$ receptors in the cytosol. q_{42} and q_{24} are the transition rates between the modes park to drive and drive to park respectively.

$$J_{SERCA} = \frac{V_{SERCA}([Ca^{2+}])^2 - \overline{k}([Ca_{ER}])^2}{K_{SERCA}^2 + ([Ca^{2+}])^2} \tag{8}$$

To meet the requirement that the calcium concentration in the cytosol is significantly lower than the calcium concentration in the ER at steady state, $\overline{k}$ is chosen to be much smaller than 1. V_{SERCA} is the maximum SERCA flux from the bulk cytosol and K_{SERCA} is the half-maximal activating cytosolic Ca^{2+} concentration of SERCA.

$$J_{diff} = \omega_c([Ca]_{MAM} - [Ca^{2+}]) \tag{9}$$

where $[Ca]_{MAM}$ represents calcium concentration in MAM and ω_c is intracellular calcium diffusion rate.

The total intracellular $[Ca^{2+}]$ which is regulated by influx and out flux of plasma membrane of cell is expressed as [55],

$$J_{in} = J_{leakin} + J_{SOCC} + J_{ROCC} \tag{10}$$

$$J_{SOCC} = \frac{V_{SOCC}K_{SOCC}^4}{K_{SOCC}^4 + [Ca_{ER}]^2} \tag{11}$$

$$J_{ROCC} = V_{ROCC}[IP3] \tag{12}$$

$$J_{PM} = \frac{V_{PM}([Ca^{2+}])^2}{[Ca^{2+}]^2 + K_{PM}{}^2} \tag{13}$$

$$J_{MCU} = \frac{\frac{([Ca^{2+}])^2}{K_1}(1 + \frac{[Ca^{2+}]}{K_1})^3 exp(p_1 V_m)}{(1 + \frac{[Ca^{2+}]}{K_1})^4 + \frac{L_{MCU}}{(1 + \frac{[Ca^{2+}]}{K_2})^{2.8}}} \tag{14}$$

$$J_{NCX} = V_{NCX}\frac{C_{mito}}{[Ca^{2+}]}exp(p_2 V_m) \tag{15}$$

where V_m denotes mitochondrial membrane potential. K_1 and K_2 represent diffusion for calcium translocation by the MCU and dissociation constant for MCU activation by Ca^{2+}. J_{leakin} represents plasma membrane leak influx, V_{SOCC} is the maximum SOCC flux entering the cytosol, K_{SOCC} is the half-maximal inhibiting ER Ca^{2+} concentration of SOCC, V_{ROCC} is rate constant of ROCC, V_{PM} is the maximum plasma membrane calcium ATPase(PMCA) efflux exiting the cytosol, K_{PM} is the half-maximal activating cytosolic Ca^{2+} concentration of PMCA, V_{NCX} is rate constant of the NCX, L_{MCU} is allosteric equilibrium constant for uniporter conformations and C_{mito} is mitochondrial calcium concentration. p_1 is coefficient of MCU activity and p_2 is coefficient of NCX activity, dependence on voltage.

The terms involved in fluxes are nonlinear, and since the Ca^{2+} concentration is in small range; therefore, the proposed problem is linearised using Taylor's approximation method around the point where calcium concentration is 2 μM and nonlinear terms of Taylor's series becomes negligible.

The Eq. (1) can be rewritten after linearisation as follows:

$$\frac{\partial[Ca^{2+}]}{\partial t} = D_{Ca}\frac{\partial^2[Ca^{2+}]}{\partial x^2} - A[Ca^{2+}] + B \tag{16}$$

where A and B are constants given by

$$A = \frac{f_c}{D_{Ca}}\left[\left((1 - R_{S1})(48.12) + \frac{(1 - R_{S2})}{R_{V3}}(840.28) + 0.18 + \omega_c\right)\right] + \frac{k_j^+[B_j]_\infty}{D_{Ca}}$$

$$B = \frac{f_c}{D_{Ca}}\left[\left((1 - R_{S1})(2.56) + \frac{(1 - R_{S2})}{R_{V3}}(168) + 0.129 + \omega_c(0.3)\right)\right] + \frac{k_j^+[B_j]_\infty[Ca^{2+}]_\infty}{D_{Ca}}$$

Production rate of IP_3 is computed using [23],

$$F_{IP3,Prod} = V_{PLC}\frac{[Ca^{2+}]^2}{K_{PLC}^2 + [Ca^{2+}]^2} \tag{17}$$

here the maximal production rate of PLC is denoted by V_{PLC} which depends on dose of agonist. The sensitivity of PLC on calcium is denoted by K_{PLC}.

Due to phosphorylation of IP_3 kinase, IP_3 degradation rate is given by [23],

$$F_{IP3,deg} = k_{deg} \frac{[Ca^{2+}]^2}{K_{deg}^2 + [Ca^{2+}]^2} [IP_3] \tag{18}$$

The phosphorylation rate and half saturation constant of IP_3 are denoted by k_{deg} and K_{deg} respectively. $[IP_3]$ represents IP_3 concentration in the cytosol.

Rate of IP_3 net growth is calculated by taking difference value of IP_3 production rate and IP_3 degradation rate given by [23],

$$\frac{\partial [IP_3]}{\partial t} = F_{IP3,Prod} - F_{IP3,deg} \tag{19}$$

where $F_{IP3,Prod}$ and $F_{IP3,deg}$ are given by Eqs. (17) and (18).

Calcium dependent ATP degradation rate is calculated using [40],

$$J_{HYD} = \frac{J_{SERCA}}{2} + K_{HYD} \frac{[ATP]_c}{[ATP]_c + K_h} \tag{20}$$

J_{SERCA} is calculated using Eq. (8), where K_{HYD} is maximal rate of ATP hydrolysis, K_h is the Michaelis-Menten constant for ATP hydrolysis and $[ATP]_c$ represents cytosolic ATP concentration.

NADH production rate is computed by [40],

$$I_{AGC} = V_{AGC} \frac{[Ca^{2+}]}{K_{AGC} + [Ca^{2+}]} \frac{q_2}{q_2 + C_{mito}} exp(p_4 V_m)$$

where V_{AGC} is rate constant for NADH production, K_{AGC} is dissociation constant of calcium from AGC (aspartate-glutamate carrier) respectively. q_2 is the half-maximal activating mitochondrial Ca^{2+} concentration of the TCA and p_4 is coefficient of AGC activity dependence on voltage.

The numerical solution is obtained by variational finite element method by dividing cytosol of the hepatocyte cell into 30 elements. The variational functional of the problem (16) in discretized form is expressed by

$$I^{(e)} = \frac{1}{2} \int_{x_i}^{x_j} \left[u^{(e)'2} + \frac{1}{Dca} \frac{\partial u^{(e)2}}{\partial t} + Au^{(e)2} - 2Bu^{(e)} \right] - \mu^{(e)} \left(\frac{\sigma_{Ca}}{D_{Ca}} u_{(x=0)}^{(e)} \right) \tag{21}$$

where $\mu^{(e)}$ is one for the first element and zero for remaining elements and $u^{(e)}$ represents calcium concentration $[Ca^{2+}]$.

The elements are very small in size; therefore, for calcium concentration, shape function is assigned as following linear variation,

$$u^{(e)} = c_1 + c_2 x \tag{22}$$

The Eq. (22) can be expressed as

$$u^{(e)} = P^T C^{(e)} \tag{23}$$

here $P^T = \begin{bmatrix} 1 & x \end{bmatrix}$

and $C^{(e)} = \begin{bmatrix} c_1 \\ c_2 \end{bmatrix}$

Values of $u^{(e)}$ at nodes x_i and x_j are given by

$$u^{(e)}(x_i) = c_1 + c_2 x_i \tag{24}$$

$$u^{(e)}(x_j) = c_1 + c_2 x_j \tag{25}$$

using Eqs. (22)–(25),

$$\overline{u}^{(e)} = P^{(e)} C^{(e)} \tag{26}$$

here $P^{(e)} = \begin{bmatrix} 1 & x_i \\ 1 & x_j \end{bmatrix}$

& $\overline{u}^{(e)} = \begin{bmatrix} u_i \\ u_j \end{bmatrix}$

From Eqs. (23)–(26),

$$u^{(e)} = P^T R^{(e)} \overline{u}^{(e)} \tag{27}$$

where $R^{(e)} = P^{(e)-1} = \frac{1}{x_j - x_i} \begin{bmatrix} x_j & -x_i \\ -1 & 1 \end{bmatrix}$

The integral (21) is rewritten as

$$I^{(e)} = I_k^{(e)} + I_m^{(e)} + I_l^{(e)} - I_r^{(e)} - I_s^{(e)} \tag{28}$$

where

$$I_k^{(e)} = \frac{1}{2} \int_{x_i}^{x_j} \left[\left(P_x{}^T R^{(e)} \overline{u}^{(e)2} \right) \right] dx \tag{29}$$

$$I_m^{(e)} = \frac{1}{2} \int_{x_i}^{x_j} \frac{1}{Dca} \frac{\partial}{\partial t} \left[\left(P^T R^{(e)} \overline{u}^{(e)2} \right) \right] dx \tag{30}$$

$$I_l^{(e)} = \frac{1}{2} \int_{x_i}^{x_j} A \left[\left(P^T R^{(e)} \overline{u}^{(e)2} \right) \right] dx \tag{31}$$

$$I_r^{(e)} = \int_{x_i}^{x_j} B \left[\left(P^T R^{(e)} \overline{u}^{(e)} \right) \right] dx \tag{32}$$

$$I_s^{(e)} = \mu^{(e)} \left[\left(\frac{\sigma_{Ca}}{2D_{Ca}} P^T R^{(e)} \overline{u}^{(e)}_{(x=0)} \right) \right] \tag{33}$$

Minimising $I^{(e)}$ with respect to $\overline{u}^{(e)}$,

$$\frac{dI^{(e)}}{d\overline{u}^{(e)}} = 0$$

that is

$$\frac{dI^{(e)}}{d\overline{u}^{(e)}} = \frac{dI_k^{(e)}}{d\overline{u}^{(e)}} + \frac{dI_m^{(e)}}{d\overline{u}^{(e)}} + \frac{dI_l^{(e)}}{d\overline{u}^{(e)}} - \frac{dI_r^{(e)}}{d\overline{u}^{(e)}} - \frac{dI_s^{(e)}}{d\overline{u}^{(e)}} \tag{34}$$

which can be written as

$$\frac{dI}{d\overline{u}^{(e)}} = \sum_{e=1}^{30} \overline{M}^{(e)} \frac{dI^{(e)}}{d\overline{u}^{(e)}} (\overline{M}^{(e)})^T = 0 \tag{35}$$

where

$$\overline{M}^{(e)} = \begin{bmatrix} 0 & 0 \\ . & . \\ 0 & 0 \\ 1 & 0 \\ 0 & 1 \\ 0 & 0 \\ . & . \\ 0 & 0 \end{bmatrix}_{31\times 2} \begin{matrix} \\ \\ \\ i^{th} row \\ j^{th} row \end{matrix}, \overline{u}^{(e)} = \begin{bmatrix} u_1 \\ u_2 \\ u_3 \\ u_4 \\ . \\ . \\ u_{30} \\ u_{31} \end{bmatrix}_{31\times 1}$$

This leads to the following system of linear algebraic equations,

$$[\overline{K}]_{(31\times 31)}\overline{u} + [\overline{N}]_{(31\times 31)} \frac{\partial \overline{u}}{\partial t}_{(31\times 1)} = [\overline{F}]_{(31\times 1)} \tag{36}$$

where system matrices are represented as $\overline{K}$, $\overline{N}$ and $\overline{F}$ is characteristic vector. For solving system, the Crank-Nicolson method is used and simulated using MATLAB program.

3 Tables

The numerical data available in literature organised in Tables 1, 2, and 3 are used for simulation in the present study.

4 Results and discussion

The graphs have been plotted for calcium variation, IP_3 production, IP_3 degradation, IP_3 net growth, ATP degradation and NADH production rates for standard values of $\sigma_{Ca}=15$ pA, $D_{ca}=200$ $\mu m^2 s^{-1}$ and buffer=10 μM from Figs. 2, 3, 4, 5, and 6.

Figure 2 displays calcium distribution along space and time in a hepatocyte cell. Figure 2A shows calcium variation along space. It is noticed from the graph that concentration of calcium is high at the source and on moving away along spatial dimension, the concentration of calcium starts decreasing and approaches towards its equilibrium state that is 0.1 μM. Maximum value of calcium concentration can be seen as 0.35 μM in this case. The nonlinear shape of the curve at different positions remain almost same. Figure 2B shows calcium variation with respect to time. Initially, the calcium concentration increases sharply with increase in time for the first ~25 ms, and then it increases gradually and smoothly to attain steady state in ~50 ms.

Figure 3 shows IP_3 production and degradation rate with respect to space and time. Figure 3A shows IP_3 production rate along the space. IP_3 production rate is largest at the source and on moving along with space coordinate, and then it starts decreasing and

Table 1 Physiological parameters for calcium variation [11, 55]

Symbol	Parameter	Value
D_{Ca}	Diffusion coefficient of $[Ca^{2+}]$	100–200 $\mu m^2/s$
RS_1	The Surface area ratio of ER and MAM	0.15
RS_2	Proportion adjoining MAM	0.15
RV_3	The volume ratio of cytosol and Mitocondria	15
ω_c	Intracellular calcium diffusion rate	0.001 s^{-1}
f_c	Fraction of free calcium	0.01
k_{IPR}	ER flux rate	0.3 s^{-1}
V_{SERCA}	Maximum SERCA flux rate	30 $\mu M s^{-1}$
K_{SERCA}	Half maximal rate of SERCA	0.35 μM
$\overline{K}$	Concentrating power of the ATPase	1×10^{-8}
V_{MCU}	Coefficient of MCU rate	0.00001 $\mu M s^{-1}$
V_{NCX}	Coefficient of NCX flux	0.5 s^{-1}
K_1	Dissociation constant for MCU efflux	19 μM
K_2	Dissociation constant for MCU activation	0.38 μM
p_1	Coefficient of voltage dependent MCU activity	0.1 mV
p_2	Coefficient of voltage dependent NCX activity	0.016 mV
V_{SOCC}	SOCC flux rate	0.8 $\mu M s^{-1}$
V_{ROCC}	ROCC flux rate	0.25 $\mu M s^{-1}$
K_{SOCC}	Half-maximal rate of SOCC	100 μM
V_{PM}	The maximal PMCA efflux	0.2 $\mu M s^{-1}$
K_{PM}	Half maximal rate of PMCA	0.45 μM
k_j^+	Buffer association rate	1.5 $\mu M^{-1} s^{-1}$

becomes 0.06 $\mu M/s$ at the other end. The nonlinear behaviour of IP$_3$ production rate profile is similar to calcium variation profile in Fig. 2A. Figure 3B shows IP$_3$ production rate with respect to time. IP$_3$ production rate increases sharply for the first ~25 ms, and then it increases smoothly and gradually to achieve steady state in ~50 ms. The temporal behaviour of IP$_3$ production rate in Fig. 3B is similar to temporal behaviour of calcium in

Table 2 Physiological parameters for IP$_3$ production and degradation, ATP degration and NADH production rate [23, 40, 56, 57]

| Symbol	Parameter	Value
V_{PLC}	Maximal-rate of PLC	$0.3 \mu M s^{-1}$
K_{PLC}	Half-activation constant of PLC	$0.2 \mu M$
k_{deg}	IP3 degradation rate constant via phosphorylation	$0.5 s^{-1}$
K_{deg}	Half-activation constant of IP3 kinases	$0.1 \mu M$
V_{AGC}	Rate constant of NADH production	$25 \mu M s^{-1}$
K_{AGC}	Dissociation constant of Ca^{2+} from AGC	$0.14 \mu M$
C_m	Mitochondrial calcium concentration	$1.3 \mu M$
V_M	Mitochondrial membrane potential	$160 mV$
ATP_c	Cytosolic ATP concentration	$0.1 \mu M$

Table 3 Physiological parameters for obesity simulation [55]

Parameter	Normal condition	Obesity
RS_1	0.15	0.3
RS_2	0.15	0.3
V_{MCU}	$0.00001\,\mu Ms^{-1}$	$0.000013\,\mu Ms^{-1}$
k_{IPR}	$0.3\ s^{-1}$	$0.35\ s^{-1}$
$\overline{K}$	1×10^{-8}	1.25×10^{-8}

Fig. 2B. Figure 3C shows IP$_3$ degradation rate with respect to space. The maximum value is obtained at the source and decreases to 0.04 $\mu M/s$ on moving away from the source. The nonlinear behaviour of IP$_3$ degradation rate is similar to calcium profile and IP$_3$ production rate in Figs. 2A and 3A. Figure 3D shows temporal IP$_3$ degradation rate. The IP$_3$ degradation rate initially increases sharply for the first ~25 ms, and then it increases smoothly and gradually to achieve steady state in ~50 ms. The temporal IP$_3$ degradation rate has similar behaviour to calcium profile and IP$_3$ production rate as seen in Figs. 2B and 3B.

Figure 4 shows IP$_3$ net growth rate along with space and time. Figure 4A is plotted with respect to space. It is observed that initially net growth rate is larger and on moving away from the source, it approaches to 0.16 $\mu M/s$. There is a change in the nonlinear behaviour of the curve compared to that in Fig. 2A. Figure 4B shows temporal IP$_3$ net growth rate. From the curves, it is seen that the net growth rate increases more gradually and smoothly compared to temporal calcium profile in Fig. 2B.

Figure 5 shows ATP degradation rate along with space and time. Figure 5A shows ATP degradation rate with respect to space. At the source, ATP degradation rate is high and starts decreasing on moving away from the source. The nonlinear behaviour of the curve is the same as Figs. 2A and 3A. Figure 5B shows ATP degradation rate with respect to time. Initially, ATP degradation rate increases sharply for the first 25 ms and then increases gradually and sharply to attain steady state at 50 ms. The temporal behaviour of ATP degradation rate is similar to that of temporal calcium variation as seen in Fig. 2B.
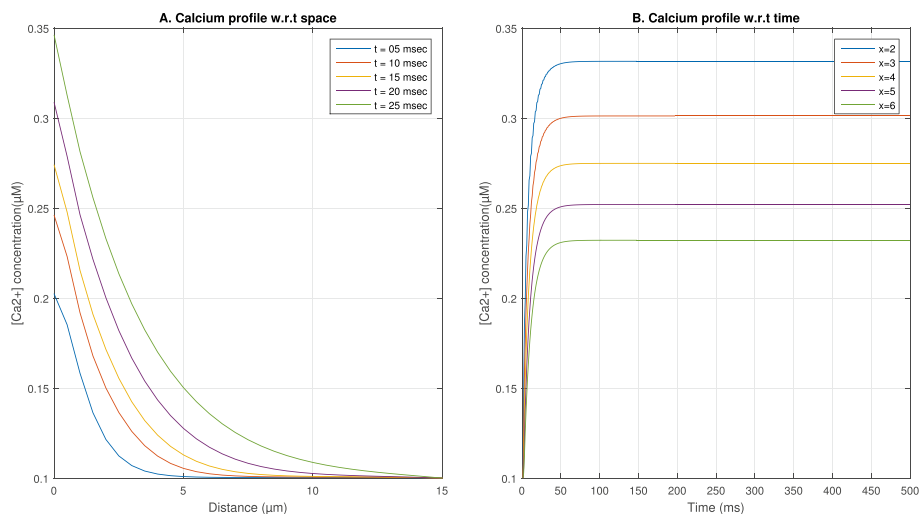
Fig. 2 Calcium distribution with $\sigma_{Ca} = 15\ pA$, $D_{ca} = 200\ \mu m^2 s^{-1}$ and buffer $= 10\ \mu M$
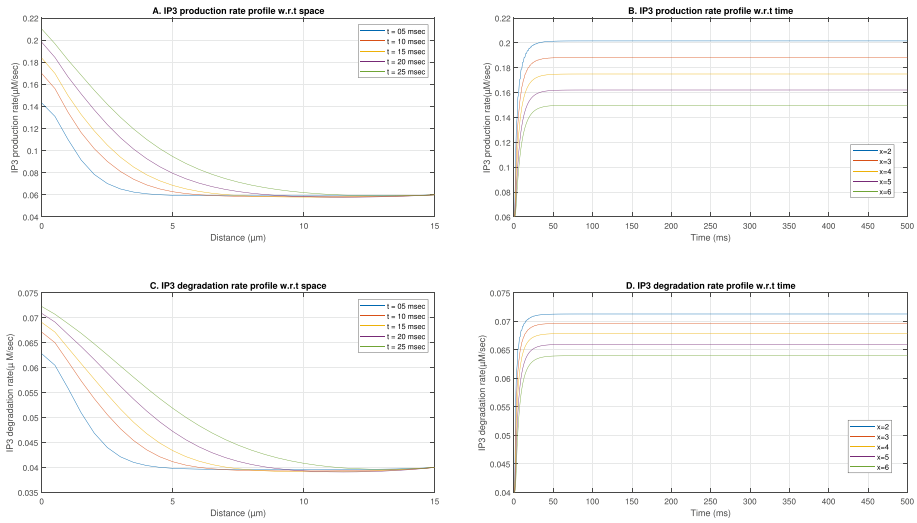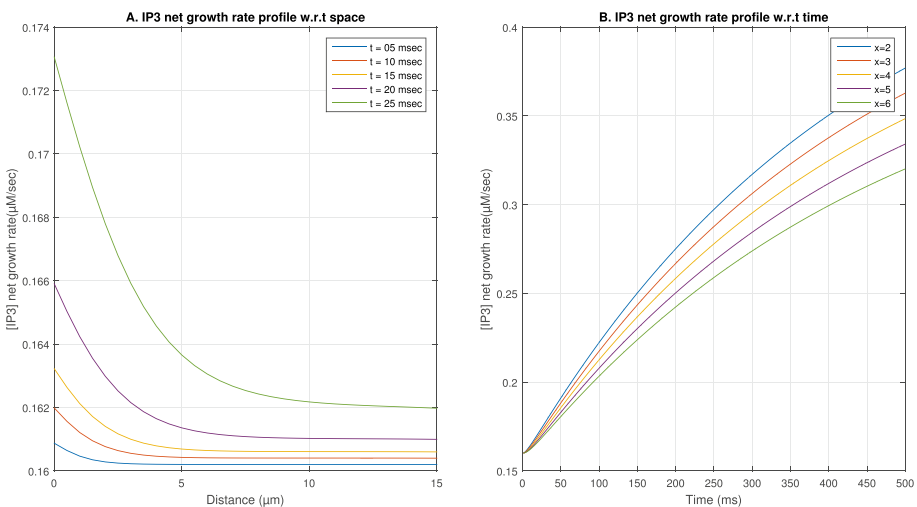
Fig. 3 IP$_3$ Production and degradation rate with $\sigma_{Ca} = 15 \ pA$, $D_{ca} = 200 \ \mu m^2 s^{-1}$ and buffer $= 10 \ \mu M$

Figure 6 shows NADH production rate along with space and time. Figure 6A shows spatial NADH production rate. When the calcium concentration is high, NADH production rate is high and on moving away from the source it reaches to a fixed point ~3.8 $\mu M/s$. The nonlinear behaviour of the curve is similar to that of calcium variation in Fig. 2A. Figure 6B shows NADH production rate with respect to time. Initially, NADH production rate increases sharply for the first 25 ms and then increases gradually and smoothly to attain steady state at 50 ms. The temporal behaviour of NADH production rate is similar to temporal behaviour of calcium variation as seen in Fig. 2B.

Fig. 4 IP$_3$ net growth rate with $\sigma_{Ca} = 15 \ pA$, $D_{ca} = 200 \ \mu m^2 s^{-1}$ and buffer $= 10 \ \mu M$
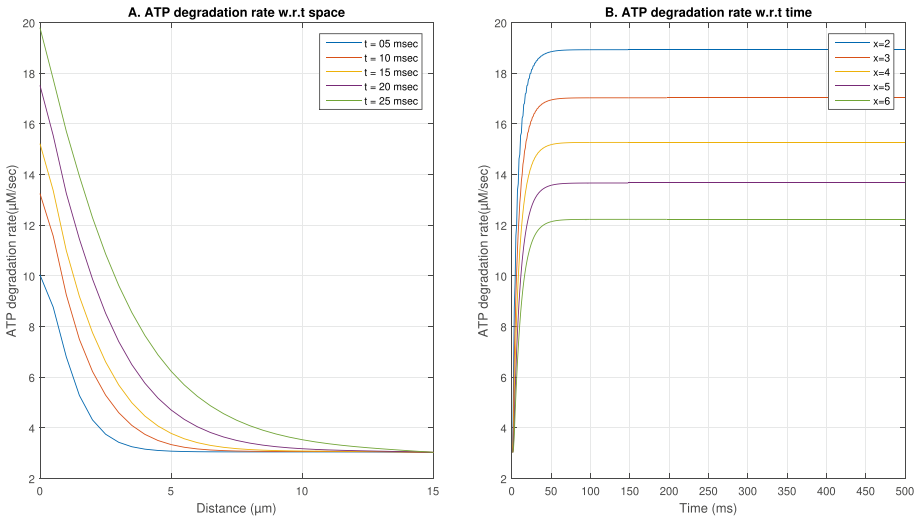
Fig. 5 ATP degradation rate with $\sigma_{Ca} = 15$ pA, $D_{ca} = 200$ $\mu m^2 s^{-1}$ and buffer $= 10$ μM

Variation with different values of source influx Graphs for calcium variation, IP_3 production rate, IP_3 degradation rate, IP_3 net growth rate, ATP degradation rate and NADH production rate are observed for diffusion coefficient $= 200$ $\mu m^2 s^{-1}$, buffer $= 10$ μM and different source influxes $= 5, 10, 15, 20$ and 25 pA respectively from Figs. 7 to 10.

Figure 7 displays calcium variation with respect to space and time. Figure 7A shows the calcium variation with respect to space. It is noticed that calcium concentration increases with the increase of source influx. The curves are smoother than Fig. 2A. Figure 7B shows temporal calcium variation for various values of source influxes. Curves of Fig. 7B behave
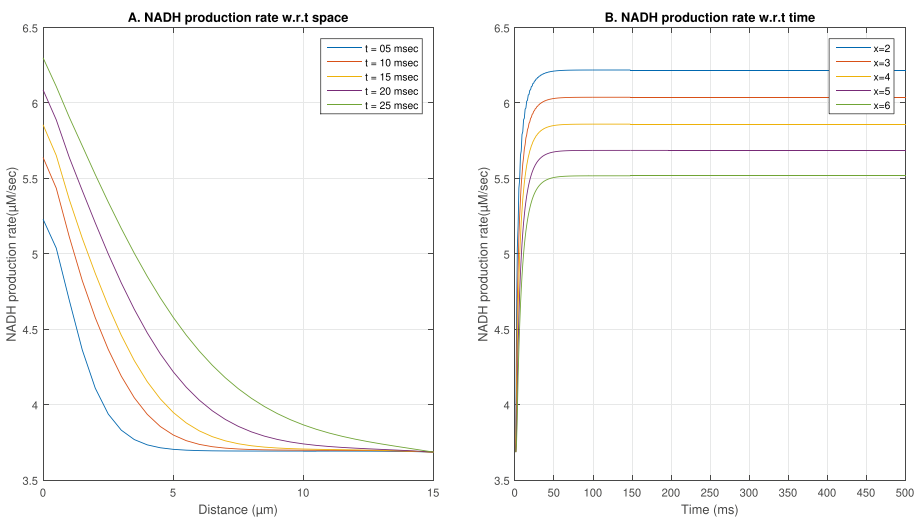
Fig. 6 NADH production rate with $\sigma_{Ca} = 15$ pA, $D_{ca} = 200$ $\mu m^2 s^{-1}$ and buffer $= 10$ μM
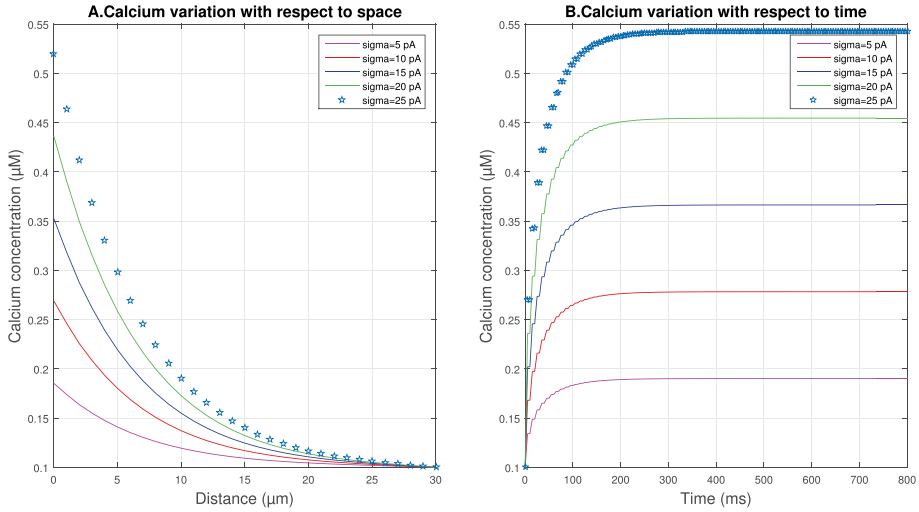
Fig. 7 Calcium distribution with buffer $= 10 \ \mu M$, $D_{ca} = 200 \ \mu m^2 s^{-1}$, source influxes $= 5, 10, 15, 20$ and 25 pA respectively

similar to Fig. 2B. Oscillations are also observed in temporal calcium variation due to some mismatches in the regulating mechanisms, during initial time period. Initially, concentration grows sharply and then increases gradually and smoothly to achieve steady state at 100 ms. The time of achieving steady state has increased to 100 ms in Fig. 7B in place of 50 ms in Fig. 2B due to increase of source influx.

Figure 8 displays IP_3 net growth, production and degradation rate along space and time. Figure 8A shows spatial IP_3 net growth rate variation. IP_3 net growth rate increases with
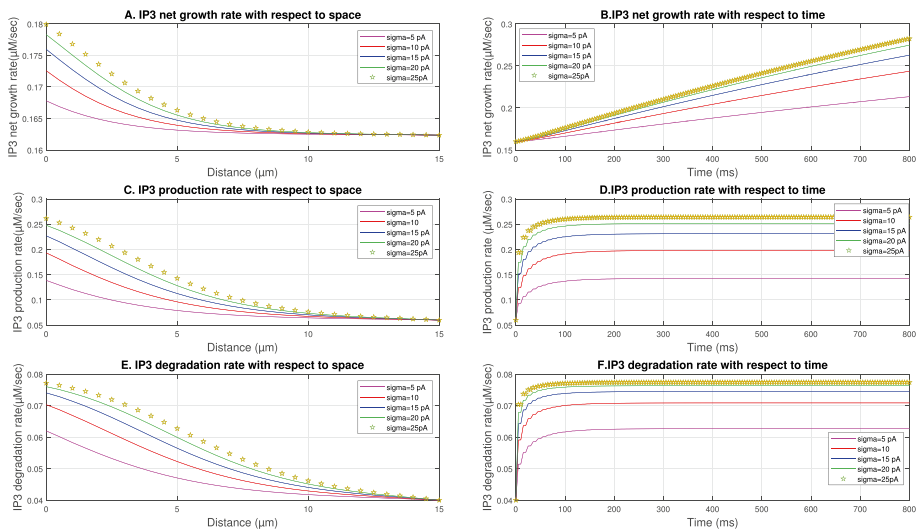
Fig. 8 IP_3 Net growth, production and degradation rate with buffer $= 10 \ \mu M$, $D_{ca} = 200 \ \mu m^2 s^{-1}$, source influxes $= 5, 10, 15, 20$ and $25 \ pA$ respectively

the increased source influx. Curves are more smoother but the behaviour of the curves is similar to that of calcium variation in Fig. 6A. Figure 8B shows IP$_3$ net growth rate with respect to time. IP$_3$ net growth rate is increasing more gradually and smoothly. Curves of Fig. 8B is similar to Fig. 4B. Figure 8C shows change in IP$_3$ production rate with respect to space. As the source influx increases, the IP$_3$ production rate also increases. When the source influx is low then IP$_3$ production rate is also low, i.e., around $0.07 \mu M/s$. The ratio of IP$_3$ production rate and source influx is different from ratio of calcium concentration and source influx. This is due to nonlinear relationship between IP$_3$ production rate and calcium concentration. The behaviour of the curves is similar to that of calcium variation in Fig. 3A. Figure 8D shows change in IP$_3$ production rate with respect to time. Initially, the IP$_3$ production rate grows sharply and then increases gradually and smoothly to attain steady state at 100 ms. Oscillations are observed in the curves due to some mismatches in the regulating mechanisms, during initial time period. The temporal behaviour of the IP$_3$ production rate is similar to that of calcium variation in Fig. 3B. Figure 8E shows IP$_3$ degradation rate with respect to space. As the source influx increases, IP$_3$ degradation rate increases, and on moving away from the source, it reaches to $0.04 \mu M/s$. Slight change in the behaviour is observed as compared to Ca^{2+} profile when moving away from the source. The ratio of IP$_3$ degradation rate and source influx is different from the ratio of calcium concentration and source influx; this is due to nonlinear relationship between IP$_3$ degradation rate and calcium concentration. Figure 8F shows IP$_3$ degradation rate with respect to time. Initially, IP$_3$ degradation rate grows sharply for the first 50 ms and then increases gradually and smoothly to attain steady state at 100 ms. Oscillations are observed in the curves due to some mismatches in the regulating mechanisms, during initial time period. The temporal behaviour of the IP$_3$ degradation rate is similar to that of calcium variation as seen in Fig. 3D.

Figure 9 shows ATP degradation rate along space and time. Figure 9A shows degradation rate of ATP with respect to space. As the calcium concentration is high near source, ATP degradation rate is high and reaches a fixed value ($\sim 4 \mu M/s$) as calcium
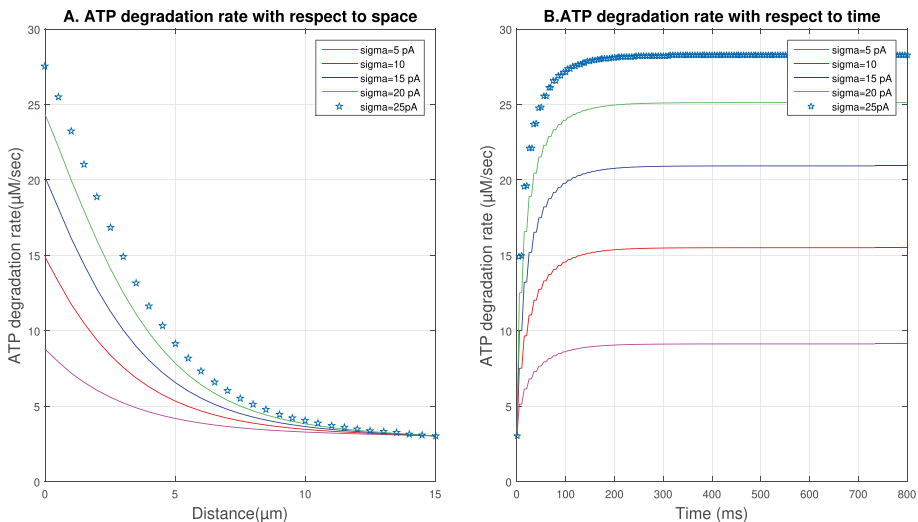

Fig. 9 ATP degradation rate with buffer $= 10 \mu M$, $D_{ca} = 200 \mu m^2 s^{-1}$, source influxes $= 5, 10, 15, 20$ and $25 \, pA$ respectively
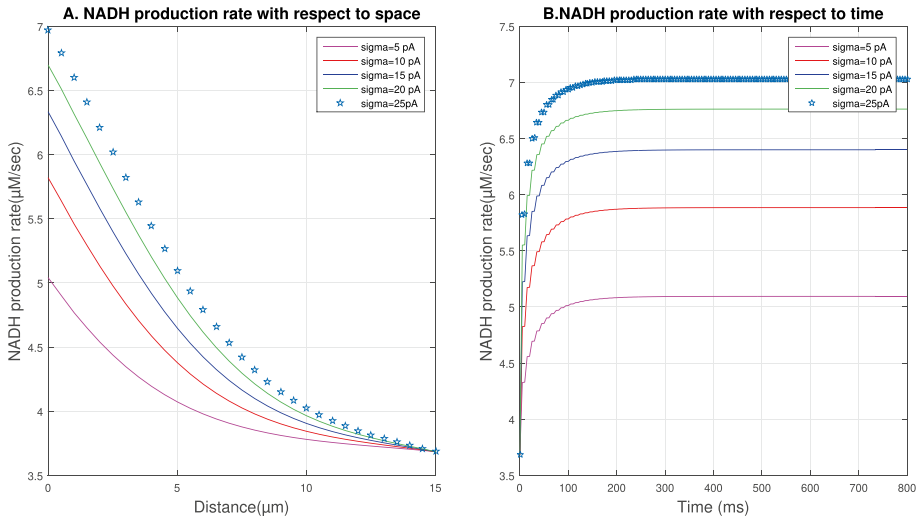
Fig. 10 NADH production rate with buffer $= 10\ \mu M$, $D_{ca} = 200\ \mu m^2 s^{-1}$, source influxes $= 5, 10, 15, 20$ and $25\ pA$ respectively

concentration reaches to its equilibrium state. Figure 9B shows ATP degradation rate with respect to time. When the source influx was high, degradation rate was high; therefore, it takes more time to reach the steady state. Ratio of growth in ATP degradation rate and behaviour of the curves is similar to that of Fig. 7A. Figure 9B shows temporal ATP degradation rate. Initially, ATP degradation rate increases sharply for the first 100 ms and then increases gradually and smoothly to reach steady state at 300 ms. Oscillations are observed in the curves due to some mismatches in the regulating mechanisms, during initial time period. The temporal behaviour of the ATP degradation rate is similar to that of calcium variation as seen in Fig. 7B.

Figure 10 shows NADH production rate along space and time. Figure 10A shows production rate of NADH with respect to space. It is observed that when the source influx is high, NADH production rate is high. As calcium reaches equilibrium state, NADH production rate reaches to some fixed value $\sim 3.7\mu M/s$. The ratio of increase in NADH production rate and behaviour of the curves is similar to that of Fig. 7A. Figure 10B shows NADH production rate with respect to time. Initially, NADH production rate increases sharply for the first 100 ms and then increases gradually and smoothly to reach steady state at 300 ms. Oscillations are observed in the curves due to some mismatches in the regulating mechanisms, during initial time period. The temporal behaviour of the NADH production rate is similar to that of calcium variation as seen in Fig. 7B.

Variation with different values of buffer The graphs have been plotted for calcium variation, IP$_3$ production rate, IP$_3$ degradation rate, IP$_3$ net growth rate, ATP degradation rate and NADH production rate with diffusion coefficient $= 200\ \mu m^2 s^{-1}$, source influx $= 5\ pA$ and different buffer values $= 5, 10, 20, 40$ and $80\ \mu M$ respectively from Figs. 11, 12, 13, and 14.

Figure 11 shows calcium distribution along space and time. Figure 11A shows calcium variation with respect to space. It is seen from the curves that with increasing value of buffer, the Ca^{2+} concentration starts decreasing as buffers bind to free calcium ions and
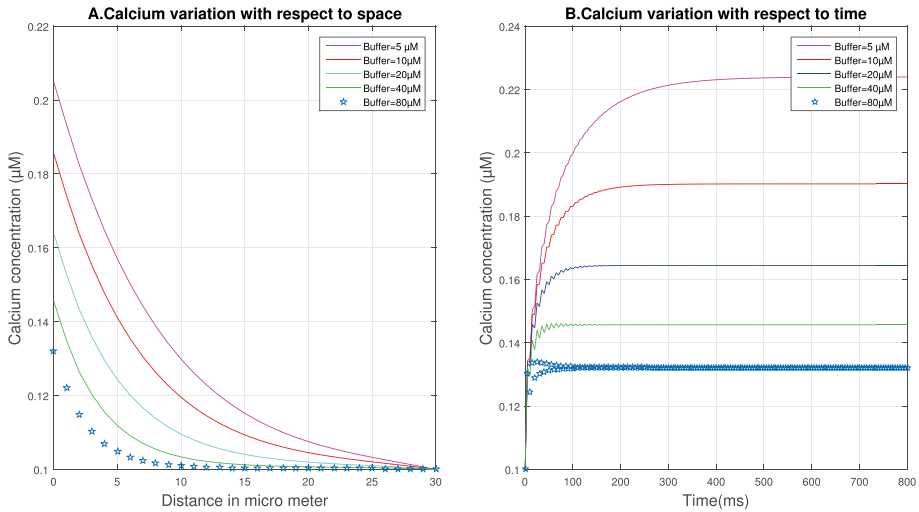
Fig. 11 Calcium distribution with source influx = 5 pA, D_{ca} = 200 $\mu m^2 s^{-1}$, buffer = 5, 10, 20, 40 and 80 μM respectively

form calcium bound buffers with respect to space and on moving from the source reaches to its equilibrium. The curves of Fig. 11A is similar to that of Fig. 2A. Figure 11B represents temporal calcium variation. It is observed that the concentration of calcium increases sharply for the first 50 ms and then increases gradually and smoothly to attain steady state at 100 ms. Oscillations are observed in the temporal curves of calcium variation due to some mismatches in the regulating mechanisms, during initial time period. The curves of Fig. 11B is similar to that of Fig. 2B.
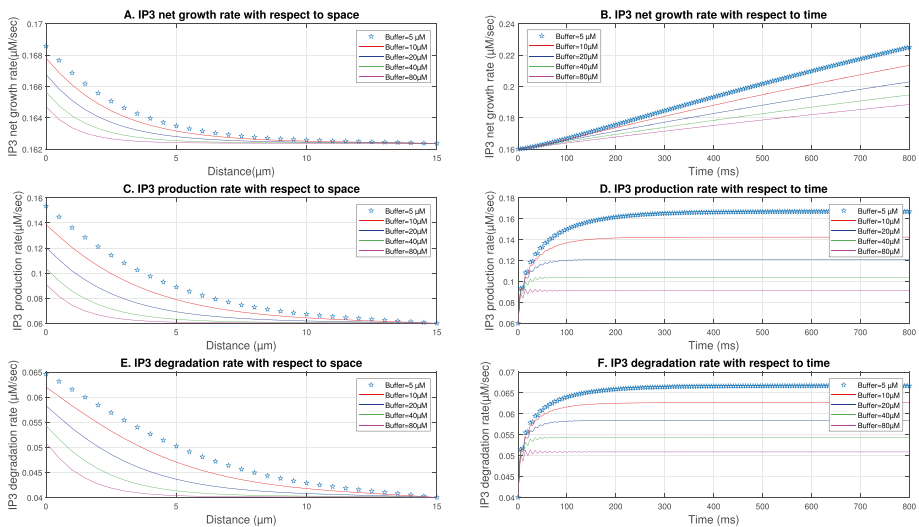

Fig. 12 IP$_3$ net growth, production and degradation rate with D_{ca} = 200 $\mu m^2 s^{-1}$, source influx = 5 pA, buffer = 5, 10, 20, 40 and 80 μM respectively
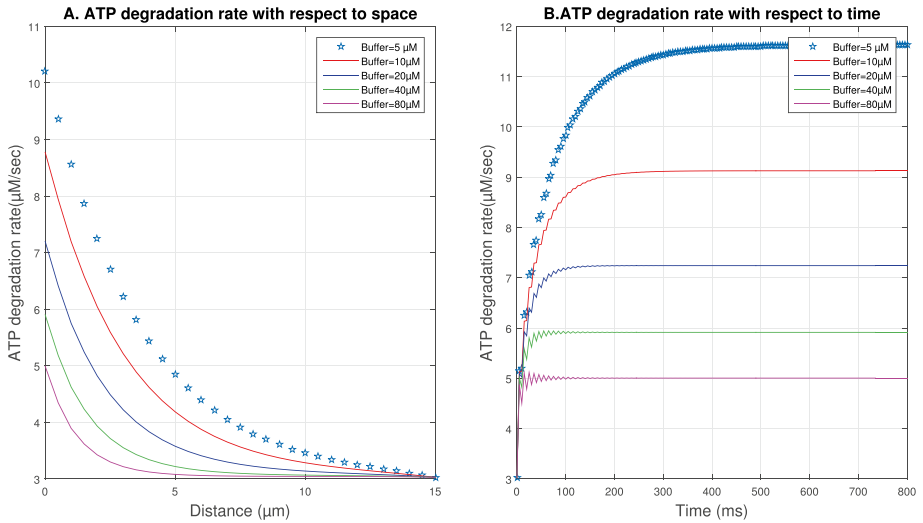
Fig. 13 ATP degradation rate with $D_{ca} = 200 \ \mu m^2 s^{-1}$, source influx = 5 pA, buffer = 5, 10, 20, 40 and 80 μM respectively

Figure 12 shows spatio-temporal IP$_3$ net growth, production and degradation rate. Figure 12A shows change in IP$_3$ net growth rate with respect to space. When the value of buffer is high, IP$_3$ net growth rate is low and with decreasing value of buffer, IP$_3$ net growth rate is increasing. Curves are more smoother but behaviour of the curve is similar to that of Fig. 11A. Figure 12B shows change in IP$_3$ net growth rate with respect to time. Curves are increasing more gradually and smoothly. Similar behaviour of the curves is observed as that in Fig. 4B. Figure 12C shows IP$_3$ production rate with respect to space.
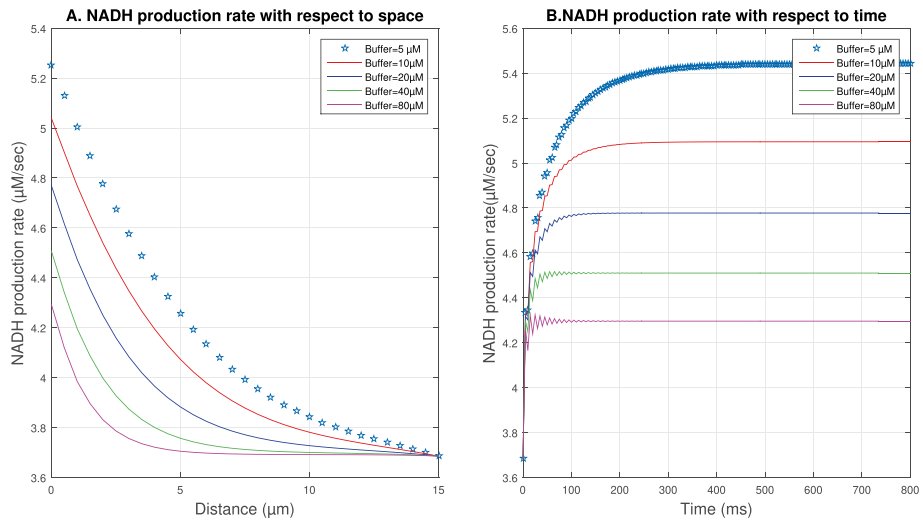

Fig. 14 NADH production rate with $D_{ca} = 200 \ \mu m^2 s^{-1}$, source influx = 5 pA, buffer = 5, 10, 20, 40 and 80 μM respectively

When the buffer value is high, IP_3 production rate is low and when buffer value is low then IP_3 production rate is high. Behaviour of the curves in Fig. 12C is similar to calcium variation as seen in Fig. 11A. Figure 12D shows IP_3 production rate with respect to time. Initially, IP_3 production rate grows sharply for the first 100 ms and then increases gradually and smoothly to attain steady state at 400 ms. Oscillations are observed in the curves due to some mismatches in the regulating mechanisms, during initial time period. The temporal behaviour of IP_3 production rate is same as that of calcium variation in Fig. 11B. Figure 12E shows IP_3 degradation rate with respect to space. It is observed from the graph that when the buffer value is low, IP_3 degradation rate is high and it increases with decreasing value of buffer. Curves are more smoother than that of Fig. 11A. Maximum value is $0.065 \mu M/s$. Moving along space dimension, IP_3 degradation rate value is decreasing and reaches to $0.04 \mu M/s$. Behaviour of the curves is same as seen in Fig. 11A. Figure 12F shows IP_3 degradation rate with respect to time. Initially, IP_3 degradation rate increases sharply for the first 100 ms and then increases gradually and smoothly to attain steady state at 400 ms. Oscillations are observed in the curves due to some mismatches in the regulating mechanisms, during initial time period. The temporal behaviour of IP_3 degradation rate is same as that of calcium variation as seen in Fig. 11B.

Figure 13 shows ATP degradation rate along space and time. Figure 13A shows ATP degradation rate with respect to space. It is observed that when the value of the buffer is high, the ATP degradation rate is decreasing and increases with decreasing value of buffer. As calcium attains equilibrium state, then ATP degradation rate attains a fixed value of $\sim 3 \mu M/s$. Behaviour of the curves in Fig. 13A is similar to that observed in Fig. 11A for calcium profiles. Figure 13B shows ATP degradation rate with respect to time. Initially, ATP degradation rate grows sharply for the first 100 ms and then increases gradually and smoothly to attain steady state at 400 ms. Oscillations are observed in the curves due to some mismatches in the regulating mechanisms, during initial time period. The temporal behaviour of ATP degradation rate is similar to calcium variation as seen in Fig. 11B.

Figure 14 shows spatio-temporal NADH production rate. Figure 14A shows production rate of NADH with respect to space. It is observed that when the buffer value is high, NADH production rate is low and as buffer decreases NADH production rate increases. The curves of Fig. 14A is similar to that of calcium variation in Fig. 11A. Moving along space dimension NADH production rate value decreases and attains some fixed value $\sim 3.7 \mu M/s$. Figure 14B shows NADH production rate with respect to time. Initially, NADH production rate increases sharply with increasing value of buffer for the first 100 ms then increases gradually and smoothly to attain steady state at 400 ms. Oscillations are observed in the curves due to some mismatches in the regulating mechanisms, during initial time period. The temporal behaviour of NADH production rate is similar to calcium variation as seen in Fig. 11B.

Comparative study in normal hepatocyte cell and obese hepatocyte cell The following graphs have been plotted for calcium variation in normal and obese conditions. Difference graphs for calcium variation, IP_3 production rate, IP_3 degradation rate, IP_3 net growth rate, ATP degradation rate and NADH production rate are plotted to understand the changes in these processes due to obesity.

Figure 15 shows calcium variation when diffusion coefficient is 200 $\mu m^2 s^{-1}$, source influx is 15 pA and buffer value is 5 μM. Figure 15A shows the calcium distribution in normal hepatocyte cell with respect to space. Graphs have been plotted for different values of time-step which are t=10 ms, 70 ms, 145 ms and 245 ms respectively. It is observed
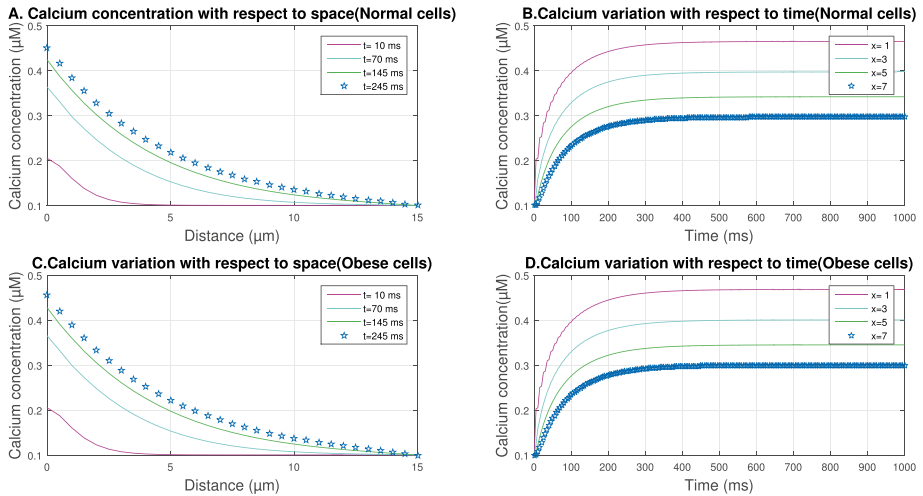
Fig. 15 Calcium variation with $D_{ca} = 200\ \mu m^2 s^{-1}$, source influx $= 15\ pA$, buffer $= 5\ \mu M$ respectively for normal cells and obese cells

from the graph that calcium concentration was initially high, and on moving away from the source, it reaches to equilibrium condition ($0.1\mu M$). Maximum calcium concentration reaches to 0.45 μM. Curves of Fig. 15A are more smoother than that of Fig. 2A, but the behaviour of both the curves is similar. Figure 15B shows calcium variation in normal hepatocyte cell with respect to time at different nodal points that are $x = 1, 3, 5$ and $7\ \mu m$ respectively. It is observed that initially, concentration is increasing sharply for the first 500 ms, and then it is increasing gradually and smoothly to attain a steady state at ~600 ms. Figure 15C is plotted under obesity condition with respect to space. Similar behaviour of calcium oscillation is observed with a small change in values as compared to Fig. 15A. Figure 15D represents temporal calcium variation due to obesity. It is seen that initially, concentration was increasing sharply for the first 500 ms, and then it is increasing gradually and smoothly to attain the steady state at ~600 ms. The behaviour of the curves seen in Fig. 15D is similar to Fig. 2B with some difference of magnitude.

Figure 16 represents difference in calcium variation in obesity and normal condition. Figure 16A, B are plotted with diffusion coefficient $= 200\mu m^2 s^{-1}$, source influx is $15pA$ and buffer value is 5 μM. In Fig. 16A, it is noticed that the difference in Ca^{2+} concentration is maximum at source and increases along time dimension and decreases along the space dimension. It is observed that initially, there was minor difference in the values of calcium concentration, but it gradually increases with the increase in time. On moving away from the source, it is reaching to zero. Difference curve of calcium variation attains a peak at the source. Figure 16B is plotted with respect to time. The difference curves are observed in Fig. 16B are more sharp than that curves of Fig. 2B. The behaviour of these curves become more gradual and smooth at 400 ms and reaches steady state after 700 ms as seen in Fig. 2B.

Figure 17 shows difference in IP$_3$ net growth, production and degradation rate in case of normal and obesity conditions with respect to space and time. Figure 17A represents difference in IP$_3$ production rate between obesity and normal condition with respect to space. It can be observed that near the source, difference is highest and increases with
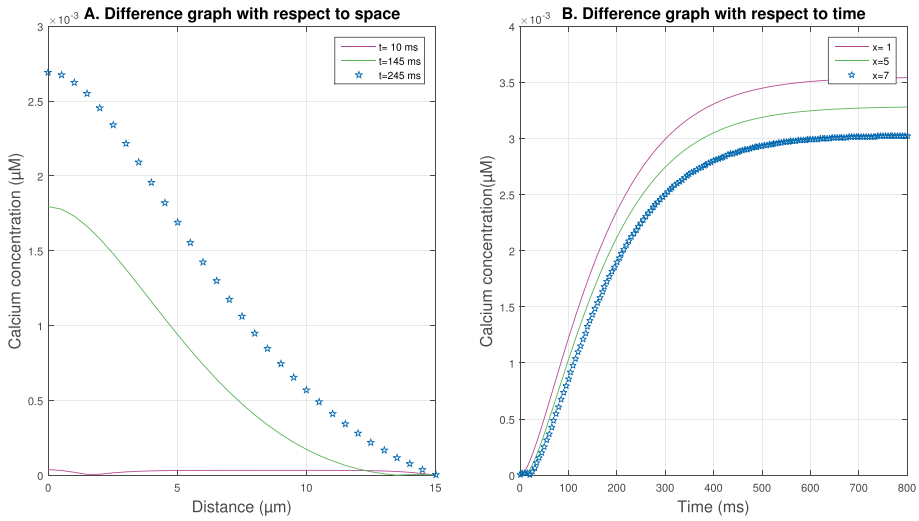
Fig. 16 Difference in calcium variation between obese and normal hepatocyte cells

increase in time. The difference is decreasing along the spatial dimension. It attains a peak at 5 μm. A slight shift in the peak is observed in difference of IP$_3$ production rate than that of calcium variation in Fig. 16A but the bell shape is similar with difference of magnitude. The shift in peak of difference curve of IP$_3$ production rate is due to the higher activity of internal stores like ER and mitochondria leading to higher fluxes of calcium from internal stores impacting the IP$_3$ production rate. Figure 17B is plotted with respect to time. Initially, rates grow sharply for the first 200 ms and increases
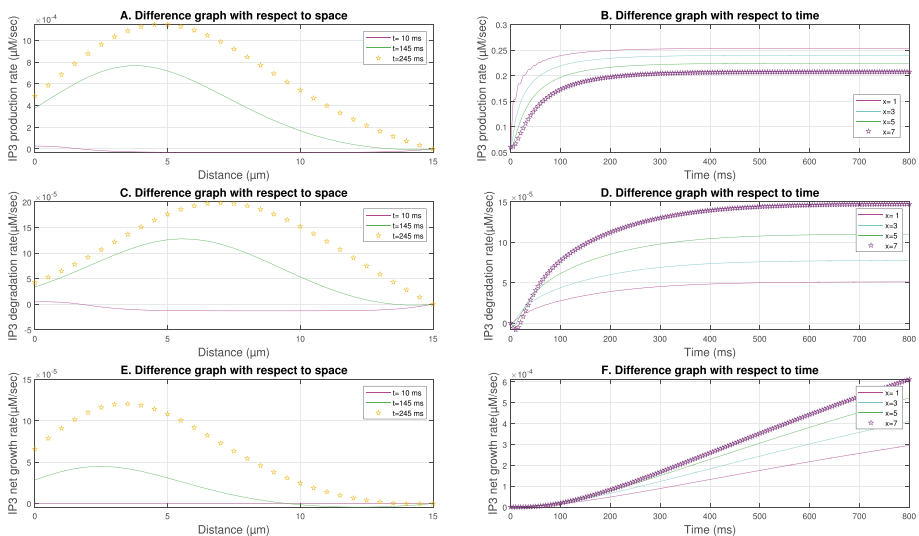

Fig. 17 Difference in IP$_3$ net growth, production and degradation rate between obese and normal hepatocyte cells with respect to space and time
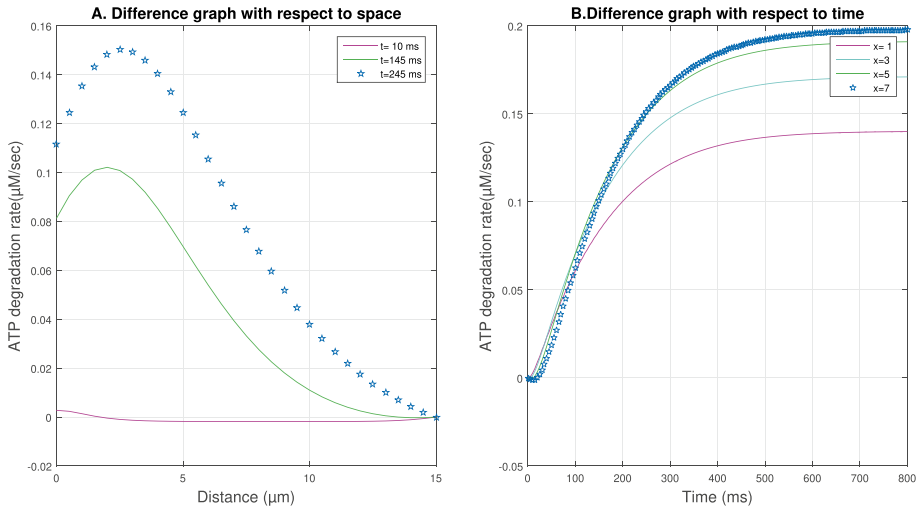
Fig. 18 Difference in of ATP degradation rate between obese and normal hepatocyte cells with respect to space and time

gradually and smoothly to attain steady state at 500 ms. Steady state is attained sooner than that in Fig. 16B. The behaviour of the curves is similar to that of calcium variation as seen in Fig. 2B. Figure 17C shows difference in IP_3 degradation rate with respect to space. The difference in IP_3 degradation rate increases with increase in time and distance from source and attains peak at 7 μm and then decreases along spatial dimension. A considerable shift in the peak is observed in difference of IP_3 degradation rate than that of calcium variation in Fig. 16A. Figure 17D shows difference in IP_3 degradation rate with respect to time. The difference in IP_3 degradation rate grows sharply upto 300 ms and then grows gradually and smoothly to achieve steady state at 700 ms. Behaviour of the graph is similar to that in Fig. 16B. Figure 17E shows difference in IP_3 net growth rate with respect to space. Near the source difference is larger and increases with increasing time and it is decreasing along with spatial coordinate. The difference curve is bell shaped. A slight change in peak is observed than that of Fig. 16A. Peak is attained at 3 μm. Figure 17F shows difference in IP_3 net growth rate with respect to time. At initial node, the difference in net growth rate is increasing smoothly and becomes sharper with increases in time.

Figure 18 shows difference in ATP degradation rate along space and time. It is observed from the Fig. 18A that at initial time-step, the difference is low, increases with higher time-step and decreases on moving along space coordinate. The peak of the curve is closer to the source as compared to Fig. 17A and attains peak at 3 μm. Behaviour of the curves is similar to that of calcium variation difference curves in Fig. 16A. Figure 18B shows difference in ATP degradation rate with respect to time. Initially, the ATP degradation rate grows sharply upto 300 ms then increases more gradually and smoothly to achieve steady state at 700 ms.

Figure 19 shows difference in NADH production rate for normal and obesity conditions along space and time. Figure 19A shows difference in NADH production rate with respect to space. Near the source, the difference is high and increases with increase in time and decreases on moving along the space coordinate. A peak is attained at 5 μm for Fig. 19A
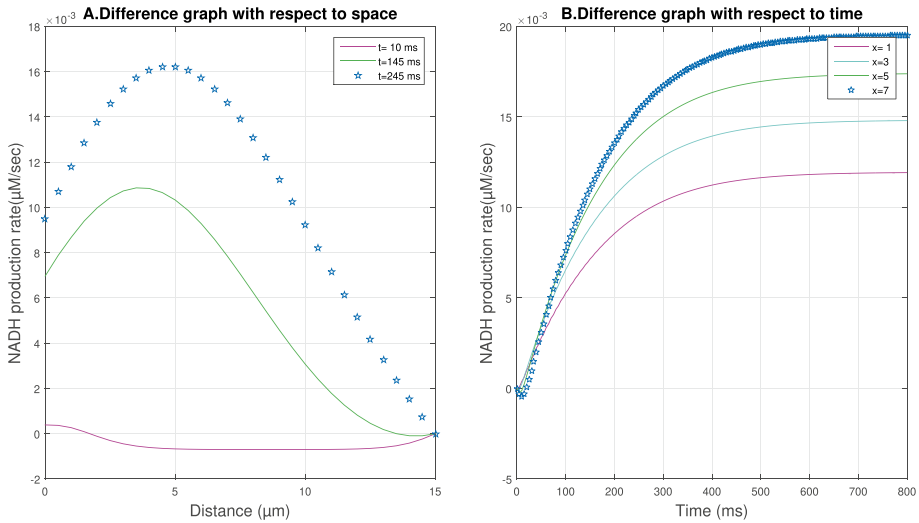
Fig. 19 Difference in NADH production rate between obese and normal hepatocyte cells with respect to space and time

which is similar to that in Fig. 17A but different from that in Figs. 17C and 18A. Figure 19B shows temporal difference curves for NADH production rate. Initially, NADH production rate grows sharply for the first 400 ms and the increases gradually and smoothly to attain steady state at 700 ms. The behaviour of the curves is similar to that of calcium variation as seen in Fig. 2B.

4.1 Error and stability analysis

Error analysis is done for t= 0.1, 0.2, 0.3, 0.4 and t=0.5 s at x=0. It can be observed from the Table 4 that maximum percentage error between number of nodes 20 and number of nodes 30 is 0.1453%. Accuracy for simulation can be concluded as ~ 99.8547%. Therefore, 30 elements are chosen for the study. The method is stable as the spectral radius for finite element method is 0.9590 which is less than 1. The methods have been found to be truly effective in the present study as the accuracy was found to be 99.8547%, and the stability of the solution was successfully established.

Table 4 Error estimation

Time	Node=20	Node=30	Absolute error	Relative error	Relative % error
0.1 s	0.346486804	0.345983942	0.000502862	0.001453425	0.145342465
0.2 s	0.363261081	0.36341837	0.000157289	0.000432805	0.043280451
0.3 s	0.365746318	0.366002175	0.000255857	0.000699058	0.069905847
0.4 s	0.366141139	0.36641229	0.000271151	0.000740015	0.074001515
0.5 s	0.366204617	0.366478265	0.000273648	0.000746698	0.07466977

Table 5 $[Ca^{2+}]$ concentration profiles compared with Peglow et al. [58] at $t=50$ s

Distance	$[Ca^{2+}]$ (Peglow)	$[Ca^{2+}]$ (present work)	Absolute error	Relative % error
x=0 μm	0.302433473	0.30123763	0.001195844	0.396976925
x=0.5 μm	0.260661503	0.258604315	0.002057187	0.682911855
x=1 μm	0.249294538	0.247739235	0.001555303	0.516304519
x=1.5 μm	0.239121848	0.236584565	0.002537283	0.842286342
x=2 μm	0.23002896	0.231480878	0.001451918	0.481984222
x=15 μm	0.1	0.1	0	0

4.2 Validation

The concentration profile of Ca^{2+} which were obtained for the parameter at $x=0$, 0.5, 1, 1.5, 2 and 15 μm are compared to earlier research by Peglow et al. [58] at time $t = 50$ s, and findings are in good accord, as demonstrated in Table 5.

5 Conclusion

The mechanisms of calcium dynamics, IP_3 production, degradation and net growth rates, ATP degradation rate and NADH production rate have been modelled successfully for normal and obese hepatocyte cell in this work. The numerical simulation was performed using finite elements for spatial dimension and Crank-Nicolson along time dimension. The obtained results agree with the dynamics of biological phenomenon occurring in the cell [59–61]. The following conclusions were made from the results of numerical simulation:

(i) The source influxes and buffers are the effective mechanisms for changing calcium concentration in a hepatocyte.

(ii) The source influx also influences the IP_3 production, degradation, net growth rates, ATP degradation rate and NADH production rate by elevating these rates on increasing source influx.

(iii) The buffers also causes the fall in IP_3 production, degradation, net growth rates, ATP degradation rate and NADH production rate on increasing buffer concentration in a hepatocyte.

(iv) The impact of source influx and buffer on calcium dynamics is transferred to the production and degradation rates of IP_3, ATP and NADH which is evident from the results.

(v) The proposed model is effective in providing the information about the response time of the cell in achieving the maximal calcium concentration, IP_3 production, degradation, net growth rate, ATP degradation rate and NADH production rate in the form of time required by each of these processes achieves steady state. The response time of each of these processes is different in different conditions.

(vi) The calcium concentration, IP_3 production, degradation, net growth rate, ATP degradation rate and NADH production rate are higher in obese hepatocytes as compared to normal hepatocytes. One of the main causes for this phenomenon is the high level of activity of internal stores and their components like ER, MCU and mitochondria leading to rise in the concentration of Ca^{2+} and IP_3 production, degradation, net growth rate, ATP degradation rate and NADH production rate. The mathematical model is

able to effectively show the impacts of dysfunction of the ER leading to obesity. The present model can be further extended to study the effects of ER dysfunction leading to the development of hypertension, insulin resistance, hyperlipidaemia, diabetes mellitus, elevated plasma insulin concentration [52], apoptosis and cell death [53].

Author contribution In terms of problem conception, solution, data correction/literature review and interpretation of the results, both writers equally contributed to this paper. The author (1) built the MATLAB code for simulation.

Data availability Not applicable

Declarations

Conflict of interest The authors declare no competing interests.

References

1. Junqueira, L.C., Mescher, A.L.: Junqueira's Basic Histology: Text & Atlas. New York [etc.]: McGraw-Hill Medical (2013)
2. Boyer, T.D., Manns, M.P., Sanyal, A.J.: Zakim and Boyer's Hepatology: a Textbook of Liver Disease. Saunders, Philadelphia, PA (2012)
3. Gaspers, L.D., Thomas, A.P.: Calcium signaling in liver. Cell Calcium **38**(3–4), 329–342 (2005). https://doi.org/10.1016/j.ceca.2005.06.009
4. Joshi, H., Jha, B. K., Dave, D. D.: Mathematical model to study the effect of mitochondria on Ca^{2+} diffusion in Parkinsonic nerve cells. In AIP Conference Proceedings (Vol. 1975, No. 1, p. 030013) (2018), AIP Publishing LLC. https://doi.org/10.1063/1.5042183
5. Contreras, L., Drago, I., Zampese, E., Pozzan, T.: Mitochondria: the calcium connection. Biochim. Biophys. Acta (BBA) Bioenerg. **1797**(6–7), 607–618 (2010). https://doi.org/10.1016/j.bbabio.2010.05.005
6. Pacher, P., Thomas, A.P., Hajnóczky, G.: Ca^{2+} marks: miniature calcium signals in single mitochondria driven by ryanodine receptors. Proc. Natl. Acad. Sci. U.S.A. **99**(4), 2380–2385 (2002). https://doi.org/10.1073/pnas.032423699
7. Naik, P.A., Pardasani, K.R.: One dimensional finite element model to study calcium distribution in oocytes in presence of VGCC, RyR and buffers. J. Med. Imag. Health Inform. **5**(3), 471–476 (2015)
8. Kotwani, M., Adlakha, N.: Modeling of endoplasmic reticulum and plasma membrane Ca^{2+} uptake and release fluxes with excess buffer approximation (EBA) in fibroblast cell. Int. J. Comput. Mater. Sci. Eng. **6**(01), 1750004 (2017). https://doi.org/10.1142/S204768411750004X
9. Jha, B.K., Adlakha, N., Mehta, M.N.: Finite element model to study calcium diffusion in astrocytes. Int. J. Pure Appl. Math. **78**(7), 945–955 (2012)
10. Panday, S., Pardasani, K.R.: Finite element model to study effect of advection diffusion and Na^+/Ca^{2+} exchanger on Ca^{2+} distribution in oocytes. J. Med. Imag. Health Inform. **3**(3), 374–379 (2013). https://doi.org/10.1166/jmihi.2013.1184
11. Jagtap, Y., Adlakha, N.: Numerical study of one-dimensional buffered advection-diffusion of calcium and IP_3 in a hepatocyte cell. Netw. Model. Anal. Health Inform. Bioinform. **8**(1), 25 (2019)
12. Jha, A., Adlakha, N.: Finite element model to study the effect of exogenous buffer on calcium dynamics in dendritic spines. Int. J. Model. Simul. Sci. Comput. **5**(02), 1350027 (2014). https://doi.org/10.1142/S179396231350027X
13. Jha, A., Adlakha, N.: Two-dimensional finite element model to study unsteady state Ca^{2+} diffusion in neuron involving ER LEAK and SERCA. Int. J. Biomath. **8**(01), 1550002 (2015). https://doi.org/10.1142/S1793524515500023
14. Pathak, K.B., Adlakha, N.: Finite element model to study calcium signalling in cardiac myocytes involving pump, leak and excess buffer. J. Med. Imag. Health Inform. **5**(4), 683–688 (2015). https://doi.org/10.1166/jmihi.2015.1443
15. Manhas, N., Pardasani, K.R.: Modelling mechanism of calcium oscillations in pancreatic acinar cells. J. Bioenerg. Biomembr. **46**, 403–420 (2014). https://doi.org/10.1007/s10863-014-9561-0
16. Atri, A., Amundson, J., Clapham, D., Sneyd, J.: A single-pool model for intracellular calcium oscillations and waves in the Xenopus laevis oocyte. Biophys. J. **65**(4), 1727–1739 (1993)

17. Isshiki, M., Ando, J., Korenaga, R., Kogo, H., Fujimoto, T., Fujita, T., Kamiya, A.: Endothelial Ca^{2+} waves preferentially originate at specific loci in caveolin-rich cell edges. Proceedings of the National Academy of Sciences **95**(9), 5009–5014 (1998). https://doi.org/10.1073/pnas.95.9.5009

18. Salet, C., Moreno, G., Vinzens, F.: Effects of photodynamic action on energy coupling of Ca^{2+} uptake in liver mitochondria. Biochem. Biophys. Res. Commun. **115**(1), 76–81 (1983). https://doi.org/10.1016/0006-291X(83)90970-1

19. Berridge, M.J., Bootman, M.D., Lipp, P.: Calcium--a life and death signal. Nature **395**(6703), 645–648 (1998). https://doi.org/10.1038/27094

20. Nicholls, D.G.: Mitochondria and calcium signaling. Cell Calcium **38**(3–4), 311–317 (2005). https://doi.org/10.1016/j.ceca.2005.06.011

21. Selwyn, M.J., Dawson, A.P., Dunnett, S.J.: Calcium transport in mitochondria. FEBS letters **10**(1), 1–5 (1970)

22. Jha, A., Adlakha, N., Jha, B.K.: Finite element model to study effect of Na^+-Ca^{2+} exchangers and source geometry on calcium dynamics in a neuron cell. J. Mech. Med. Biol. **16**(02), 1650018 (2016). https://doi.org/10.1142/S0219519416500184

23. Manhas, N., Anbazhagan, N.: A mathematical model of intricate calcium dynamics and modulation of calcium signalling by mitochondria in pancreatic acinar cells. Chaos Solitons Fractals **145**, 110741 (2021). https://doi.org/10.1016/j.chaos.2021.110741

24. Tewari, S., Pardasani, K. R.: Finite element model to study two dimensional unsteady state cytosolic calcium diffusion in presence of excess buffers. IAENG Int. J. Appl. Math. **40**(3), 108–112 (2010). https://doi.org/10.14317/jami.2011.29.12.427

25. Tewari, S.G., Pardasani, K.R.: Modeling effect of sodium pump on calcium oscillations in neuron cells. J. Multiscale Model. **4**(03), 1250010 (2012). https://doi.org/10.1142/S1756973712500102

26. Tewari, S.G., Majumdar, K.K.: A mathematical model of the tripartite synapse: astrocyte-induced synaptic plasticity. J. Biol. Phys. **38**, 465–496 (2012). https://doi.org/10.1007/s10867-012-9267-7

27. Brumen, M., Fajmut, A., Dobovišek, A., Roux, E.: Mathematical modelling of Ca^{2+} oscillations in airway smooth muscle cells. J. Biol. Phys. **31**, 515–524 (2005). https://doi.org/10.1007/s10867-005-2409-4

28. Das, P.N., Kumar, A., Bairagi, N., Chatterjee, S.: Effect of delay in transportation of extracellular glucose into cardiomyocytes under diabetic condition: a study through mathematical model. J. Biol. Phys. **46**, 253–281 (2020). https://doi.org/10.1007/s10867-020-09551-8

29. Das, P.N., Halder, S., Bairagi, N., Chatterjee, S.: Delay in ATP-dependent calcium inflow may affect insulin secretion from pancreatic beta-cell. Appl. Math. Model. **84**, 202–221 (2020).

30. Das, P.N., Pedruzzi, G., Bairagi, N., Chatterjee, S.: Coupling calcium dynamics and mitochondrial bioenergetic: an in silico study to simulate cardiomyocyte dysfunction. Mol. Biosyst. **12**(3), 806–817 (2016)

31. Colman, M.A., Pinali, C., Trafford, A.W., Zhang, H., Kitmitto, A.: A computational model of spatio-temporal cardiac intracellular calcium handling with realistic structure and spatial flux distribution from sarcoplasmic reticulum and t-tubule reconstructions. PLoS Comput. Biol. **13**(8), e1005714 (2017)

32. Means, S.A., Sneyd, J.: Spatio-temporal calcium dynamics in pacemaking units of the interstitial cells of Cajal. J. Theor. Biol. **267**(2), 137–152 (2010)

33. Paul, A., Das, P.N., Chatterjee, S.: A minimal model of glucose-stimulated insulin secretion process explores factors responsible for the development of type 2 diabetes. Appl. Math. Model. **108**, 408–426 (2022)

34. Naik, P.A., Zu, J.: Modeling and simulation of spatial-temporal calcium distribution in T lymphocyte cell by using a reaction-diffusion equation. J. Bioinform. Comput. Biol. **18**(02), 2050013 (2020)

35. De Pittà, M., Goldberg, M., Volman, V., Berry, H., Ben-Jacob, E.: Glutamate regulation of calcium and IP_3 oscillating and pulsating dynamics in astrocytes. J. Biol. Phys. **35**, 383–411 (2009). https://doi.org/10.1007/s10867-009-9155-y

36. Bianchi, K., Rimessi, A., Prandini, A., Szabadkai, G., Rizzuto, R.: Calcium and mitochondria: mechanisms and functions of a troubled relationship. Biochim. Biophys. Acta Mol. Cell Res. **1742**(1–3), 119–131 (2004). https://doi.org/10.1016/j.bbamcr.2004.09.015

37. Amaya, M.J., Nathanson, M.H.: Calcium signaling in the liver. Compr. Physiol. **3**(1), 515 (2013). https://doi.org/10.1002/cphy.c120013

38. Babcock, D.F., Herrington, J., Goodwin, P.C., Park, Y.B., Hille, B.: Mitochondrial participation in the intracellular Ca^{2+} network. J. Cell Biol. **136**(4), 833–844 (1997)

39. Marhl, M., Haberichter, T., Brumen, M., Heinrich, R.: Complex calcium oscillations and the role of mitochondria and cytosolic proteins. Biosystems **57**(2), 75–86 (2000). https://doi.org/10.1016/S0303-2647(00)00090-3

40. Wacquier, B., Combettes, L., Van Nhieu, G.T., Dupont, G.: Interplay between intracellular Ca^{2+} oscillations and Ca^{2+}-stimulated mitochondrial metabolism. Sci. Rep. **6**(1), 1–16 (2016). https://doi.org/10.1038/srep19316

41. Thomas, A.P., Renard, D.C., Rooney, T.A.: Spatial and temporal organization of calcium signalling in hepatocytes. Cell Calcium **12**(2–3), 111–126 (1991). https://doi.org/10.1016/0143-4160(91)90013-5

42. Murphy, E., Coll, K., Rich, T.L., Williamson, J.R.: Hormonal effects on calcium homeostasis in isolated hepatocytes. J. Biol. Chem. **255**(14), 6600–6608 (1980). https://doi.org/10.1016/s0021-9258(18)43612-5

43. Dupont, G., Tordjmann, T., Clair, C., Swillens, S., Claret, M., Combettes, L.: Mechanism of receptor-oriented intercellular calcium wave propagation in hepatocytes. The FASEB Journal **14**(2), 279–289 (2000). https://doi.org/10.1096/fasebj.14.2.279

44. Kothiya, A., Adlakha, N.: Model of calcium dynamics regulating IP_3 and ATP production in a fibroblast cell. Adv. Syst. Sci. Appl. **22**(3), 49–69 (2022). https://doi.org/10.25728/assa.2022.22.3.1219

45. Kothiya, A., Adlakha, N.: Cellular nitric oxide synthesis is affected by disorders in the interdependent Ca^{2+} and IP_3 dynamics during cystic fibrosis disease. J. Biol. Phys. (2023). https://doi.org/10.1007/s10867-022-09624-w

46. Bhardwaj, H., Adlakha, N.: Radial basis function based differential quadrature approach to study reaction diffusion of Ca^{2+} in T lymphocyte. Int. J. Comput. Methods (2022). https://doi.org/10.1142/S0219876222500591

47. Pawar, A., Raj Pardasani, K.: Effects of disorders in interdependent calcium and IP_3 dynamics on nitric oxide production in a neuron cell. Eur. Phys. J. Plus **137**(5), 1–19 (2022). https://doi.org/10.1140/epjp/s13360-022-02743-2

48. Pawar, A., Pardasani, K.R.: Effect of disturbances in neuronal calcium and IP_3 dynamics on β-amyloid production and degradation. Cogn. Neurodyn. 1–18 (2022). https://doi.org/10.1007/s11571-022-09815-0

49. Pawar, A., Pardasani, K.R.: Simulation of disturbances in interdependent calcium and β-amyloid dynamics in the nerve cell. Eur. Phys. J. Plus **137**(8), 1–23 (2022). https://doi.org/10.1140/epjp/s13360-022-03164-x

50. Pawar, A., Pardasani, K.R.: Study of disorders in regulatory spatiotemporal neurodynamics of calcium and nitric oxide. Cogn. Neurodyn. 1–22 (2022). https://doi.org/10.1007/s11571-022-09902-2

51. Pawar, A., Pardasani, K.R.: Computational model of calcium dynamics-dependent dopamine regulation and dysregulation in a dopaminergic neuron cell. Eur. Phys. J. Plus **138**(1), 30 (2023)

52. Kopelman, P.G.: Obesity as a medical problem. Nature **404**(6778), 635–643 (2000)

53. Bullón-Vela, M. V., Abete, I., Martínez, J. A., Zulet, M. A.: Obesity and nonalcoholic fatty liver disease: role of oxidative stress in obesity, pp. 111–133 (2018). Academic Press. https://doi.org/10.1016/B978-0-12-812504-5.00006-4

54. Arruda, A.P., Pers, B.M., Parlakgul, G., Güney, E., Goh, T., Cagampan, E., Hotamisligil, G.S.: Defective STIM-mediated store operated Ca^{2+} entry in hepatocytes leads to metabolic dysfunction in obesity. Elife **6**, e29968 (2017). https://doi.org/10.7554/eLife.29968

55. Han, J.M., Periwal, V.: A mathematical model of calcium dynamics: obesity and mitochondria-associated ER membranes. PLoS Comput. Biol. **15**(8) (2019). https://doi.org/10.1371/journal.pcbi.1006661

56. Crompton, M., Moser, R., Lüdi, H., Carafoli, E.: The interrelations between the transport of sodium and calcium in mitochondria of various mammalian tissues. Eur. J. Biochem. **82**(1), 25–31 (1978). https://doi.org/10.1111/j.1432-1033.1978.tb11993.x

57. Politi, A., Gaspers, L.D., Thomas, A.P., Höfer, T.: Models of IP_3 and Ca^{2+} oscillations: frequency encoding and identification of underlying feedbacks. Biophys. J. **90**(9), 3120–3133 (2006). https://doi.org/10.1529/biophysj.105.072249

58. Peglow, M., Niemeyer, B.A., Hoth, M., Rieger, H.: Interplay of channels, pumps and organelle location in calcium microdomain formation. New J. Phys. **15**(5), 055022 (2013)

59. Naraghi, M., Neher, E.: Linearized buffered Ca^{2+} diffusion in microdomains and its implications for calculation of $[Ca^{2+}]$ at the mouth of a calcium channel. J. Neurosci. **17**(18), 6961–6973 (1997)

60. Neher, E.: The use of fura-2 for estimating Ca^{2+} buffers and Ca^{2+} fluxes. Neuropharmacology **34**(11), 1423–1442 (1995)

61. Smith, G. D.: Modeling intracellular calcium: diffusion, dynamics, and domains. In Modeling in the Neurosciences, pp. 357–392. CRC Press (2005)